UFMTrack: Under-Flow Migration Tracker enabling analysis of the entire multi-step immune cell extravasation cascade across the blood-brain barrier in microfluidic devices

Mykhailo Vladymyrov[1, 2], Luca Marchetti[1], Sidar Aydin[1, +], Sasha Soldati[1], Adrien Mossu[1], Arindam Pal[1, Δ], Laurent Gueissaz[1, ◊], Akitaka Ariga[3, □], and Britta Engelhardt[1]

[1] Theodor Kocher Institute, [2] Data Science Lab, and [3] Laboratory for High Energy Physics, University of Bern, Bern, Switzerland

present address: [+] Department of Pharmacology, University of California, San Diego; [Δ] Department of Biomedical Engineering, University of Texas at Dallas; [◊] Department of Neuroscience, Karolinska Institutet, Stockholm, Sweden; [□] Laboratory for Elementary Particle Physics, Department of Physics, Chiba University, Chiba, Japan

Correspondence:

Dr. Mykhailo Vladymyrov

Theodor Kocher Institute

University of Bern, Bern, Switzerland

mykhailo.vladymyrov@tki.unibe.ch

Authors contribution

M.V. implemented the ^{UFM}Track software framework, conducted automated analysis and performance evaluation, and contributed to experimental design and imaging.

M.V. and B.E. wrote the manuscript with contributions from S.S., S.A., and L.M.

M.V., with contributions from S.A., L.M., and S.S., conceptualized the T-cell migration analysis pipeline.

L.M., S.A., and S.S. conducted wet lab experiments and imaging.

S.A., L.M., A.M., and M.V. performed annotation of the datasets for the segmentation model training.

S.A., L.G., A.P., and M.V. performed manual data analysis.

A.A. and B.E. designed the research together with M.V., acquired funding, and coordinated the collaboration.

Abstract

The endothelial blood-brain barrier (BBB) strictly controls immune cell trafficking into the central nervous system (CNS). In neuroinflammatory diseases such as multiple sclerosis, this tight control is, however, disturbed, leading to immune cell infiltration into the CNS. The development of in vitro models of the BBB combined with microfluidic devices has advanced our understanding of the cellular and molecular mechanisms mediating the multi-step T-cell extravasation across the BBB. A major bottleneck of these in vitro studies is the absence of a robust and automated pipeline suitable for analyzing and quantifying the sequential interaction steps of different immune cell subsets with the BBB under physiological flow in vitro.

Here we present the Under-Flow Migration Tracker (^{UFM}Track) framework and a pipeline built based on it to study the entire multi-step extravasation cascade of immune cells across brain microvascular endothelial cells under physiological flow in vitro. ^{UFM}Track achieves 90% track reconstruction efficiency and allows for scaling due to the reduction of the analysis cost and by eliminating experimenter bias. This allowed for an in-depth analysis of all behavioral regimes involved in the multi-step immune cell extravasation cascade. The study summarizes how ^{UFM}Track can be employed to delineate the interactions of $CD4^+$ and $CD8^+$ T cells with the BBB under physiological flow. We also demonstrate its applicability to the other BBB models.

Author summary

Immune cells continuously travel through our body to perform immune surveillance. They travel within blood vessels at a very high speed and slow down upon reaching their target organ by the sequential interaction with different adhesion and signaling molecules on the vascular endothelial cells.

The study of molecular mechanisms mediating this multi-step extravasation of immune cells has been significantly advanced by in vitro cultures of microvascular endothelial cell monolayers. The

dynamic interaction of the immune cells with endothelial monolayers can be imaged over time in vitro in microfluidic devices under physiological flow. The manual analysis of the acquired imaging data is time-consuming and prone to experimenter error. Analysis automation is, however, hampered by the similar appearance of the unlabeled immune and endothelial cells and by the flow causing rapid immune cell displacement.

Here we introduce ^{UFM}Track, the under-flow migration tracker framework allowing for automated analysis of immune cell interactions with microvascular endothelial cells under flow in vitro. ^{UFM}Track performs comparably to the manual analysis of an experienced researcher, eliminates experimenter's bias, and improves the accuracy of the immune cell tracking. Taken together, ^{UFM}Track sets the stage for scalability of in vitro live cell imaging studies of immune cell extravasation.

Keywords

Automated analysis, blood-brain barrier, cell tracking under flow, deep learning, flow chamber, leukocyte trafficking, live cell imaging, machine learning, microfluidics, multiple sclerosis, T cell

Introduction

Immune cells continuously travel throughout our body as a means of immune surveillance. Moving within the bloodstream allows for their fast transport to even distant sites but requires extravasation once they have reached their target organ. Immune cell extravasation across the vascular wall is a multi-step process regulated by the sequential interaction of different signaling and adhesion molecules on the endothelium and the immune cells (1,2). These molecular interactions mediate distinct sequential steps, namely tethering and rolling to reduce travel speed, shear-resistant arrest, polarization and crawling of the immune cell on the luminal surface of the endothelium, and finally, immune cell diapedesis across the endothelial layer (1,3,4).

The precise molecular mechanisms mediating the multi-step immune cell extravasation in each organ depend on the immune cell subset but also the specific characteristics of the vascular bed. For example, in the central nervous system, the endothelial blood-brain barrier (BBB) establishes a tight barrier that strictly controls the transport of molecules across the BBB, ensuring tissue homeostasis required for neuronal function. The BBB similarly controls immune cell trafficking into the CNS. Thus, accounting for these special barrier properties, unique characteristics of the multi-step T-cell migration across the BBB have been described. For instance, T cells crawl for very long distances against the direction of blood flow on the surface of the BBB endothelium in search of permissive locations for diapedesis (5–7). Research on T-cell interaction with the BBB has already been successfully translated into therapies in the clinic (8,9).

Exploring the entire multi-step extravasation of immune cells across the BBB has been significantly advanced by making use of in vitro BBB models maintaining their barrier properties, and placing them into microfluidic devices (10). Combined with microscopic setups that allow for in vitro live-cell imaging of the immune cell interaction with the brain endothelial monolayer under physiological flow over time, the molecular mechanisms mediating the sequential interaction of T cells during extravasation across the BBB have been delineated (1). These studies have shown that

102 upon their arrest, T cells polarize and either crawl at speeds between 3 to 10 µm/minute over the
103 brain endothelial monolayer or probe the endothelial monolayer by remaining rather stationary and
104 sending cellular protrusions into the endothelial monolayer (11,12). Both behaviors can lead to
105 diapedesis of the T cells across the brain endothelial monolayers. This process lasts at least 3 to 5
106 minutes, with some immune cells observed to protrude and retract several times prior to finalizing a
107 prolonged diapedesis process to the abluminal side of the brain endothelial monolayer (7,13).
108 Finally, T cells that have successfully migrated across the brain endothelial monolayer usually
109 continue to migrate underneath the endothelial monolayer (14,15).

110 The data analysis of these "in vitro flow assays" requires time-consuming offline frame-by-frame
111 analysis of the imaging data by individual experimenters, in which the dynamic interactions of each
112 individual immune cell has to be followed over the entire time of the assay manually and assigned to
113 specific categories. Such analysis is tedious, and accurately assigning the different T-cell behaviors
114 requires experience. Thus, this manual analysis is prone to inevitable errors and subjective
115 judgments of the various experiments. Furthermore, the time-consuming manual T-cell tracking
116 limits the number of events that can be studied and, thus, the statistical power of the analysis.

117 Automation of the analysis of the recorded multi-step T-cell extravasation across the BBB in the
118 microfluidic device would thus be highly desirable. It is, however, hampered as these assays are
119 usually performed with unlabeled cells and imaged by phase contrast, which poses a challenge due
120 to the similar grayscales and morphology of the immune cells interacting with the brain endothelial
121 cells. Further challenges include perfused on top T cells that, in the presence of shear flow, instantly
122 appear within the field of view (FoV) and are either suddenly displaced over a certain distance or
123 completely detached and washed away. Proper analysis of these events is mandatory for reliable T-
124 cell tracking but also with respect to the study of the overall avidity of the dynamic T-cell interaction
125 steps with the underlying brain endothelium. Thus, it was compulsory to establish a tracking solution
126 that accounts for the effect of the flow on the migrating cells and the distinct migration regimes.

127 Here we introduce the developed under-flow migration tracker (^{UFM}Track) framework that
128 systematically addresses the hurdles mentioned above, allowing it to perform automated tracking
129 and analysis of cell-cell interactions. We also show a successful implementation of ^{UFM}Track to build
130 an analysis pipeline for T-cell interactions with brain microvascular endothelial cells in vitro under
131 physiological flow. ^{UFM}Track reaches 90% T-cell tracking efficiency, performing comparably to manual
132 analysis while eliminating the experimenter's bias and improving the accuracy of T-cell tracking.
133 Therefore, it enables significant savings in the labor force and time for data analysis.

134

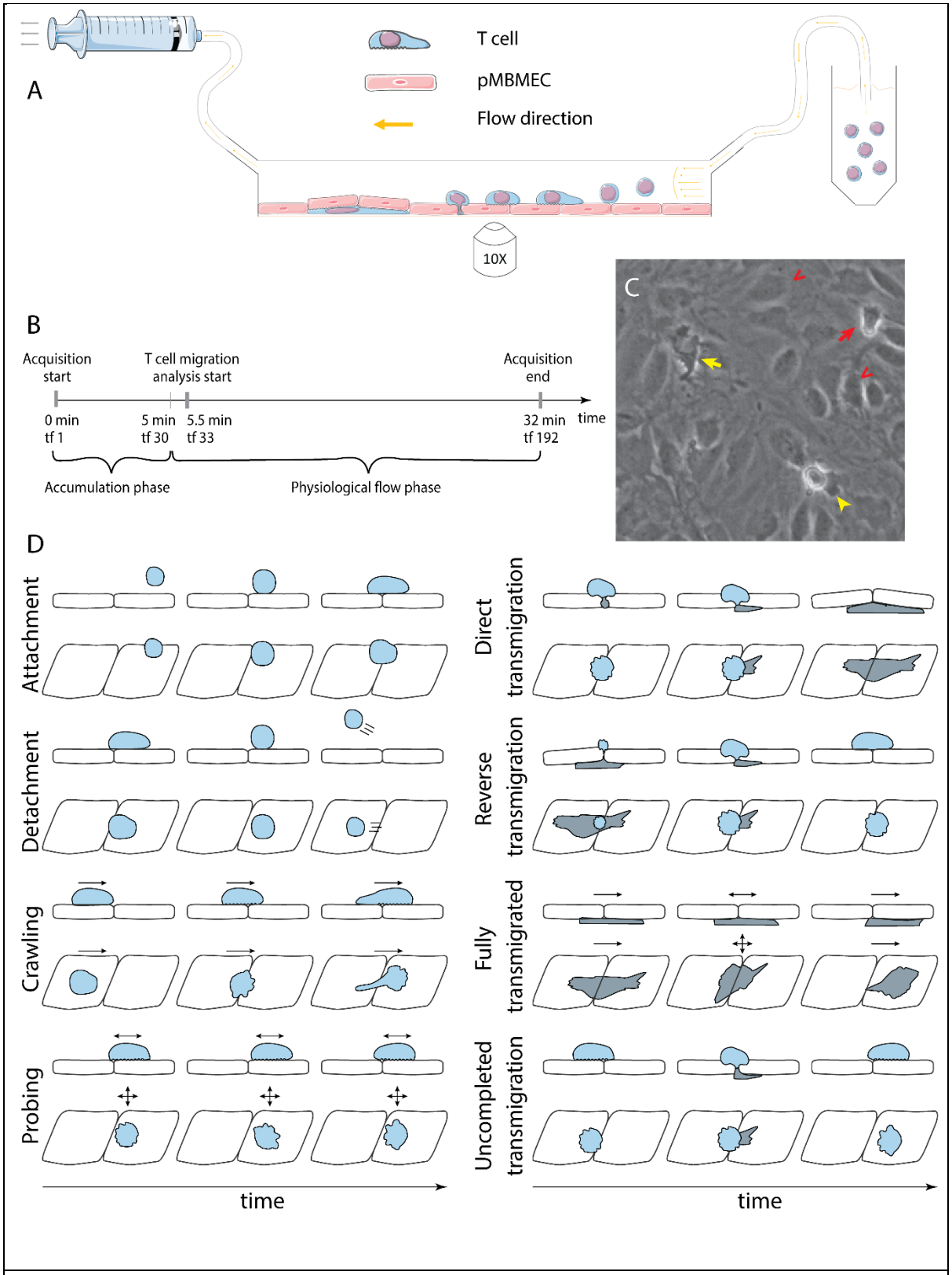

Figure 1. In vitro analysis of the multistep cascade of T-cell migration across the BBB model under physiological flow. A. In vitro under-flow assay setup. T cells were perfused on top of the pMBMEC monolayer, and their migration under flow was observed using phase-contrast imaging modality.

Imaging was performed with a time step of 10 seconds/timeframe. B. In vitro flow assay timeline. During the accumulation phase under flow with the shear stress of 0.1 dynes/cm^2, T cells adhered to the pMBMEC monolayer. After 5 minutes (timeframe 30), the shear stress was increased to 1.5 dynes/cm^2, leading to rapid detachment of not firmly adhering T cells. Analysis of the post-arrest T-cell behavior was thus starting at 5.5 minutes (timeframe 33). tf = timeframe. C. Example of phase-contrast imaging data. Red arrow – crawling T cell; yellow arrow – fully transmigrated T cell; yellow arrow-head – transmigrated part of a partially transmigrated T cell; red V arrowheads – pMBMECs. D. Schematic representation of distinct T-cell behavior regimes detected and analyzed using the developed ^{UFM}Track framework. Crawling cells migrate continuously while probing cells interact with the pMBMECs and move around the interaction point within two cell-size ($20\ \mu m$) as indicated by the arrows. Side and top views are shown.

Results

To design and develop the automated T-cell under-flow migration analysis framework ^{UFM}Track framework presented here, we made use of in vitro imaging datasets following T-cell migration across primary mouse brain microvascular endothelial cells (pMBMECs) under physiological flow in vitro. The framework combines three components: T-cell segmentation and transmigration detection, T-cell tracking under flow, and analysis of each of the multistep T-cell migration cascade steps. Segmentation and transmigration detection of the T cells, migrating on the pMBMECs, is performed with a 2D+T U-Net-like convolutional neural network (16). The T-cell under-flow tracking algorithm was formulated as a constrained optimization problem.

Next, we describe the methods and algorithms employed to develop ^{UFM}Track. Links to the code and the datasets used for model training can be found in the Data Availability section.

148

149 I. T-cell segmentation

150 Reliable cell segmentation is crucial for reliable cell tracking. In the phase-contrast imaging
151 modality, it was impossible to achieve reliable differentiation between T cells and endothelial cells of
152 the pMBMEC monolayer based on pixel intensity. For detection of T-cell transmigration across
153 pMBMEC monolayers (diapedesis), sufficiently reliable cell segmentation of the transmigrated T cells
154 was also required. To achieve this, we have designed 2D and 2D+T U-Net-like (16) fully convolutional
155 neural network-based models for multitask learning. The models were trained to predict three
156 maps: cell probability, the probability that the T cell is below the pMBMEC monolayer, and cell
157 centroids. The models performed predictions based on the grayscale of the respective phase-
158 contrast images in the case of the 2D model or sequences of 5 timeframes in the case of the 2D+T
159 model. The models were implemented in TensorFlow (17). The training was performed using the
160 annotation mask for T cells ("T cell mask") and the mask of the transmigrated part of the T cells
161 ("transmigration mask"), the centroids map, and the weight map (Figure 2). They have
162 approximately 3M and 8M parameters correspondingly, and the model architectures are
163 summarized in Supplementary Tables 1, 2. Details on models' implementation, training, and image
164 processing can be found in the "Segmentation models" section of the Supplementary Material.

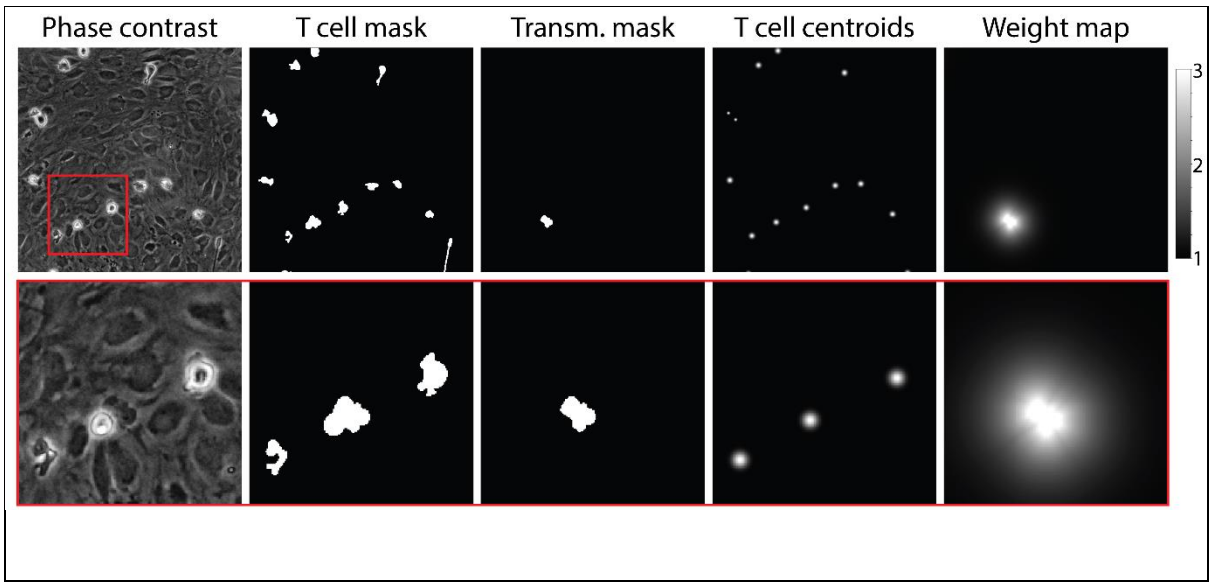

Figure 2. Example of data used for training of the T-cell segmentation model. From left to right: Phase-contrast microscopy image of T cells migrating on top of the pMBMEC monolayer; annotated T cell mask; annotated mask of transmigrated part of T cells; T cell centroids; w_{cell} weight map. The bottom row shows zoom-in on the highlighted area.

In the T cell mask prediction task, the 2D+T model outperformed the 2D model by a notable 9% according to the average precision (AP) metric (Table 1). At the same time, for the transmigration mask, which is much more difficult to infer, the 2D model performance reached only 54%, which is insufficient for reliable detection of T cells migrating across the pMBMEC monolayer. In this task, the 2D+T model outperformed the 2D model by 32% AP. We observed that the 2D+T model was sensitive to frame misalignment, leading to false positive detection of transmigrated T cells. Thus, to generate the preliminary T-cell masks used for frame alignment and histogram normalization, we employed the 2D model. Afterward, for the T-cell segmentation and transmigration detection, we employed the 2D+T model, followed by a watershed algorithm based on the inferred T-cell mask and the cell centroids as seed points. A stitched phase-contrast image sequence can be seen in Supplementary Video 1 and overlayed with the segmented cells and highlighted transmigration mask in Supplementary Video 2.

Table 1. Comparison of the performance of the 2D and 2D+T-cell segmentation models.

	Performance, AP	
	2D	2D+T
T Cell mask	86.12%	95.26%
Transmigration mask	50.56%	82.74%

181 After segmentation, we suppressed the noise by discarding small objects with an area below 30
182 pixels (the mean area of a T cell is about 400 pixels). For each T cell, we evaluated its coordinates as
183 geometric mean coordinate, angle of the longer axis, and elongation $\epsilon = \sqrt{\frac{\sum_i (x_i' - x_0')^2}{\sum_i (y_i - y_0')^2}}$,where $x_i', y_i{}'$
184 are projections of the i-th T cell mask pixel coordinates on the orthogonal long and short axes of the
185 T cell, and x_0', y_0' are the corresponding projections of the geometrical center of the T cell. The
186 summation is performed over the area covered by the mask of the corresponding T cell. Additionally,
187 we evaluated the mean T cell probability $\overline{p_{cell}} = \frac{1}{n_{pix}} \sum_i p_{cell,i}$, mean transmigration probability
188 $\overline{p_{tr}} = \frac{1}{n_{pix}} \sum_i p_{tr,i}$, and cell transmigration coefficient as $t_c = \frac{1}{n_{pix}} \sum_i \frac{\min(p_{tr,i},\ p_{cell,i})}{p_{cell,i}}$, where n_{pix} is
189 number if cell pixels and $p_{cell,i}$, $p_{tr,i}$ are the T cell and transmigration probabilities for i-th pixel in
190 the predicted T cell mask.

191

192 II. T-cell tracking

193 The presence of flow causes several types of discontinuous events that were managed with a
194 specialized tracking algorithm. These are: 1) the sudden appearance of T cells in the field of view
195 (FoV), 2) the sudden detachment of a T cell followed by its disappearance from FoV, and 3) the
196 displacement over significant distances (up to hundreds of micrometers) of T cells that do not
197 adhere firmly to the pMBMECs. The primary inspiration for our approach was the Conservation
198 Tracking algorithm (18). We could consistently reconstruct the T-cell tracks by performing global
199 optimization constrained to controlled probabilities of T-cell appearance, disappearance, and
200 displacement due to the flow at every time point. This procedure favors the reconstruction of long T-
201 cell tracks while at the same time allowing for tracking of the T cells which detach or are displaced by
202 the flow ("accelerated T-cell movement") over a longer distance ($> 8\ \mu m$) with speed significantly
203 higher than their crawling speed.

204 The tracking consists of four main steps: linking, searching for track candidates, global track
205 consistency resolving, and resolving the track intersections. At the linking step, we identified all
206 possible connections of T cells between the timeframes (Figure 3C).

207 Next, during the search for track candidates, we aimed to find continuous track segments of T
208 cells or under-segmented groups of T cells crawling on top of or below the pMBMEC monolayer
209 without accelerated movement segments on the T cell track characterized by rapid T cell
210 displacements. The whole dataset of T cells across all time points was represented as a graph. Each
211 vertex corresponds to a T cell (multiplicity m=1) or a group of potentially under-segmented T cells
212 (m>1). The vertices are connected according to links obtained at the linking step. Track segments
213 were found by performing global optimization to find consistent connectivity of vertices across the
214 time points (Figure 3D) by employing an approach inspired by the conservation tracking algorithm
215 summarized in Schiegg et al. (18). Optimization was performed using the CP-SAT constrained
216 optimization procedure using the open source OR-Tools library (19).

217 Next, resolving global track consistency was performed. In this step, the scope of T cell tracking is
218 shifted from individual nodes (representing T cells at particular timeframes as well as groups of
219 under-segmented T cells) to the track segments (unambiguous sequences of nodes) and vertices at
220 the endpoints of the segments. These are track start and end points, points of merging and
221 separation of track segments in case of under-segmentation, as well as ambiguous points on a track.
222 The latter was identified by sudden T cell displacement, a hallmark of detaching and reattaching T
223 cells and T cells transitioning from properly segmented to under-segmented T cells or vice versa
224 (Figure 3E). This was followed by the search for potential missing track segments due to accelerated
225 T cell movement under flow and missing links in the track crossing points. Both are characterized by
226 significant displacement lengths such that they were not detected during the linking step. Thus we
227 will refer to both as “jumps” in this section. We have also eliminated short and therefore unreliable
228 segments, as well as segments whose multiplicity was found to be $M = 0$ (Figure 3F). Afterward, we

229 separated the segments into two categories, namely segments with multiplicity $M = 1$, i.e., tracks of
230 isolated T cells, and segments with multiplicity $M > 1$, i.e., tracks of under-segmented groups of T
231 cells, where tracks of several T cells intersected. Finally, we extended the tracks of isolated T cells
232 into the intersection if the branching vertex had a multiplicity of n and was splitting in exactly n
233 segments with multiplicity $M = 1$ (Figure 3G).

234 Lastly, we resolved the track intersections to obtain reliable T cell tracks, i.e., identifying track
235 segments corresponding to the same T cell before and after the under-segmented track region
236 (Figure 3H).

237 Detailed information on the developed under-flow T cell tracking algorithm is given in the "T-cell
238 tracking" section of the Supplementary Material.

239 III. T-cell migration analysis

240 Next, we performed the T-cell migration analysis based on the reconstructed T cell tracks. We
241 selected tracks inside the fiducial area of the FoV, namely coordinates of the T cell at all timepoints
242 along the track were located at least 25 µm away from the bounding box enclosing all segmented T
243 cells. Next, tracks of T cells touching another T cell at the end of the assay acquisition were excluded
244 since T cells directly adjacent to each other can hide the start of T cell transmigration across the
245 pMBMEC monolayer and thus compromise correct detection and quantification of this step.
246 Additionally, only tracks with T cells were assigned in at least 6 timeframes during the physiological
247 flow phase. We also require T cells to be assigned for at least 75% of timeframes along the track.
248 Under-segmented parts of T cell tracks were not considered. Examples of selected tracks can be
249 seen in Supplementary Video 3.

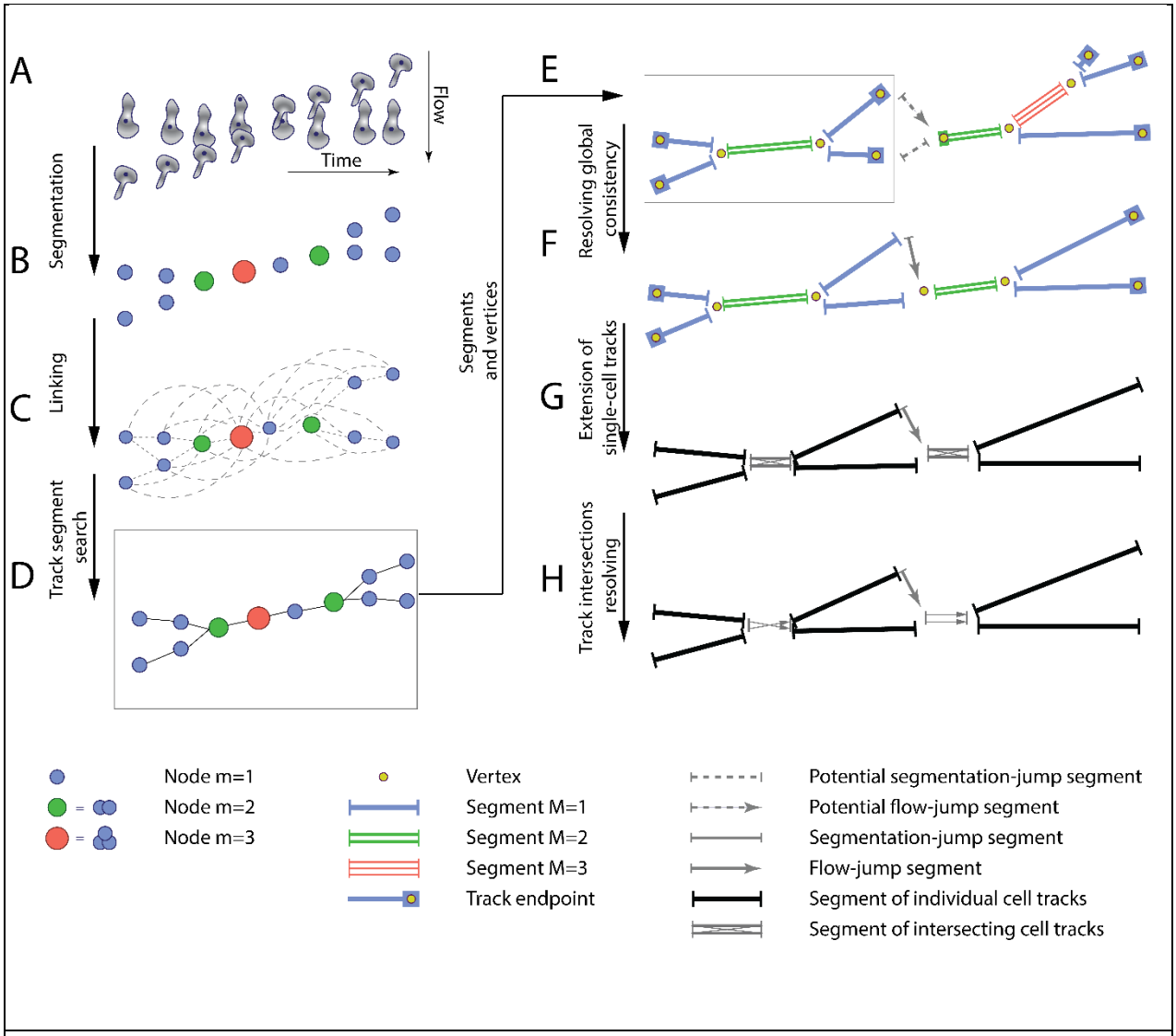

Figure 3. The T-cell tracking pipeline. A. Segmentation and centroids of two migrating T cells under flow over time. B. Nodes corresponding to segmented T cells. Node sizes and colors denote the multiplicity estimate of a node. C. Nodes, together with links between adjacent in space and time nodes, form a graph. D. Selected links are obtained with global optimization on the graph. E. Graph of segments and vertices obtained according to node multiplicity. F. Resolving global segment multiplicity consistency with global optimization on the graph. Additionally, a search for rapid displacement of segmented T cells due to under-segmentation or flow is performed. G. Extension of tracks of individual T cells into the track intersection. H. Resolving track intersections.

250

251 After exclusion of the tracks of the cellular debris, which were misclassified as T cells during the
252 segmentation step, using a dedicated “not-a-T-cell” classifier, we performed identification of
253 transmigration (Supplementary Figure 5), probing and crawling migration regimes, as well as
254 accelerated movement along the T cell track. Detailed information on the analysis of the T cell tracks
255 is given in the “T-cell migration analysis” section of the Supplementary Material.

256 Finally, for each track, we evaluated motility parameters for each of the following migration
257 regimes: probing before the transmigration, crawling before the transmigration, all crawling above
258 pMBMECs monolayer including T cell crawling segments after the first transmigration attempts, all
259 crawling below pMBMECs monolayer, whole T-cell track excluding accelerated movement and
260 tracking inefficiency regions, as well as whole T-cell track. Specifically, we evaluated the following T-
261 cell motility parameters: duration of each migration regime, the total vector and absolute
262 displacements, the migration path length, the average migration speed (displacement over time),
263 average crawling speed (path length over time), and finally the mean and standard deviation of the
264 instantaneous speed. We evaluated migration time, displacement, and average speed for the
265 accelerated movement regime.

266

267 IV. Analysis of trafficking datasets

268 Having developed a full pipeline based on the ^{UFM}Track framework for automated analysis of the
269 multi-step T-cell migration cascade across the BBB model, we next aimed to compare the results of
270 the automated analysis with previous studies, assess the capacity of the framework to gain novel
271 insight into T-cell migration under flow, and evaluate its performance as compared to manual
272 analysis.

273

274 1. $CD4^+$ T cell analysis

275 To this end, we first analyzed a total of 18 imaging datasets dedicated to understanding the
276 multi-step migration of $CD4^+$ T cells across non-stimulated (n= 6), TNF stimulated (n=5), and IL1-β-
277 stimulated (n=7) pMBMEC monolayers under physiological flow with the developed pipeline.

278 In these in vitro live cell imaging datasets, phase-contrast imaging was performed as described in
279 the "Data acquisition" section above. The T-cell accumulation phase corresponding to the shear
280 stress of 0.1 dynes/cm^2 lasted for 32 timeframes (5 minutes), followed by conditions of physiological
281 flow (shear stress 1.5 dynes/cm^2) for the subsequent 160 timeframes (27 minutes). After increasing
282 to physiological flow rates (11), a significant number of T cells detached from the pMBMEC
283 monolayers, with higher numbers of T cells detaching from non-stimulated pMBMEC monolayers
284 when compared to those stimulated with pro-inflammatory cytokines as detected by the distribution
285 of the track ending times between 5 and 30 minutes. (Figure 4A).

286 Analyzing these datasets with the established ^{UFM}Track framework, the T-cell behavior type for
287 each detected T-cell track and the aggregated T-cell behavior statistic were obtained for the
288 stimulated and non-stimulated pMBMEC monolayers (Figure 4B). The data obtained with ^{UFM}Track
289 were in accordance with our previous observations obtained by manual frame-by-frame analysis
290 (11,13,20). We further obtained the data for T-cell migration speed, T-cell displacement, and T-cell
291 path lengths for the crawling T cells, as these are the primary cell motility parameters. As shown in
292 Figure 4C-H, we observed statistically significant differences in the mean T-cell motility parameters
293 depending on the pMBMECs stimulation condition. Furthermore, we observed differences in the
294 shape of the distribution of T-cell crawling speeds, consistent with our previous reports of underlying
295 differences in the mechanisms mediating T-cell crawling on non-stimulated versus cytokine-
296 stimulated pMBMECs (20). While not statistically significant, we noted a trend towards an increased
297 variance of the T cell instantaneous speed on stimulated compared to non-stimulated pMBMECs
298 (Figure 4G). This suggests that T-cell crawling is often interrupted by T-cell recognizing specific cues
299 on the stimulated endothelium. The T cell meandering index (MI) distribution was high on non-

300 stimulated and lower on stimulated pMBMECs (Figure 4H), underscoring that cytokine stimulation
301 enhances directed T-cell movement on the pMBMEC monolayer.

302 Since the analysis was performed automatically with UFMTrack, it allowed for deeper insights into
303 the T-cell migration behavior on the pMBMEC monolayers than obtained by manual frame-by-frame
304 analysis. Specifically, the detection of accelerated movement by UFMTrack enables the researcher to
305 quantify the kinetics of individual T-cell detachment from the endothelium rather than simply
306 quantifying a bulk T-cell detachment rate. This detachment kinetics is reflected in the average speed
307 experienced during accelerated movement, which is significantly lower for the IL1-b condition
308 (Figure 4I), suggesting the need to break more bonds with the endothelium when pro-inflammatory
309 cytokines are present.

310 As our UFMTrack workflow achieves sufficient segmentation efficiency to detect T cells below the
311 pMBMEC monolayer and T-cell transmigration across the pMBMEC monolayer, it also enables
312 investigation of T-cell movement after the transmigration step. In Figure 4J, we show the distribution
313 of the migration speed for the transmigrated $CD4^+$ T cells. Interestingly, cytokine stimulation of
314 pMBMECs, although applied from the luminal side, also affected T-cell movement at the abluminal
315 side of the pMBMEC monolayer. While in the microfluidic device used in the present study, the
316 migration of T cells below the pMBMEC monolayer may not be biologically relevant, this analysis
317 option will be valuable for future studies involving multilayer in vitro BBB models that include the
318 vascular basement membrane in addition to pericytes and astrocytes to mimic the entire
319 neurovascular unit (7,21).

320 Importantly, our UFMTrack automatically detects and characterizes unusual events, such as reverse
321 T-cell transmigration, that are easily overlooked with manual counting. We do not present the
322 statistics here, as only a few such events were observed. However, when applied to the multilayer
323 BBBs in forthcoming in vitro models, systematic detection and analysis of these rare events will be
324 important to understand T-cell migration in immune surveillance.

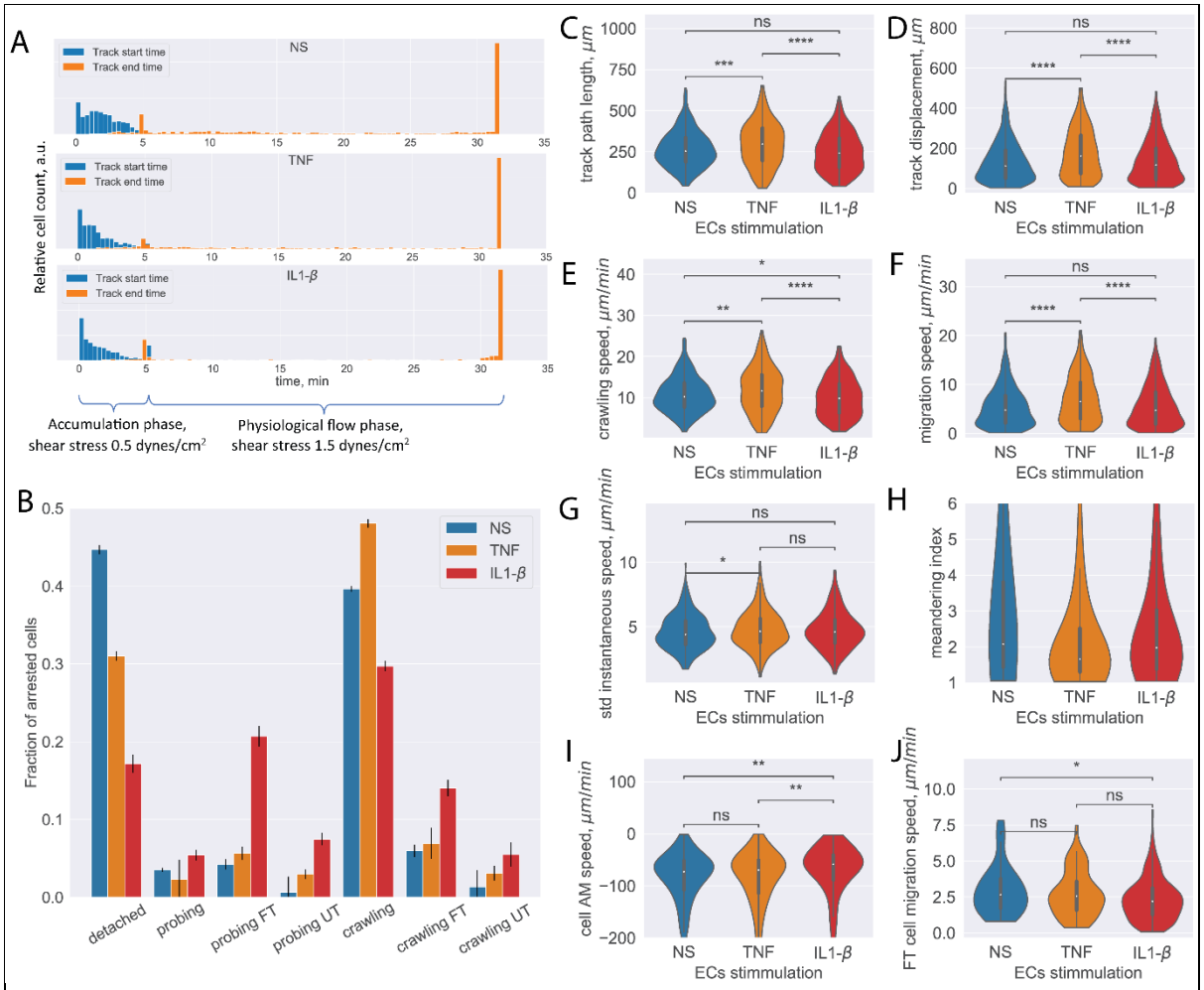

Figure 4. Analysis of CD4⁺ T-cell tracks. A. Start and end time distribution of CD4⁺ T-cell tracks on non-stimulated or TNF or IL-1β stimulated pMBMECs. More T cells detach from the non-stimulated pMBMECs after 5 minutes when the flow is increased to physiological levels. B. Quantification of CD4⁺ T-cell behavior in the respective categories obtained on non-stimulated and TNF and IL-1β stimulated pMBMECs. Error bars show the statistical error of the mean. (see text for details). C-H. Motility parameters of the crawling CD4⁺ T cells were obtained for the three endothelial stimulatory conditions. Distributions of T-cell path length (C), displacement (D), crawling speed (path/time) (E), migration speed (displacement/time) (F), variability of instantaneous T-cell crawling speed along the track (standard deviation, G), and meandering index (H). I. Distribution of CD4⁺ T-cell accelerated movement (AM) speed is a proxy metric for the T-cell

adhesion to the healthy or inflamed endothelium. J. Migration speed distribution of the transmigrated $CD4^+$ T cells. Stimulation applied to the luminal side of pMBMECs affects T-cell migration at the abluminal side of pMBMECs after their transmigration.

FT - T cells performed full transmigration; UT – T cells performed uncompleted transmigration.

2. $CD8^+$ T cells analysis

As we have previously shown that the multi-step T-cell extravasation across pMBMEC monolayers differs between $CD4^+$ and $CD8^+$ T cells, we next analyzed two datasets studying the multi-step migration of $CD8^+$ T cells across non-stimulated (NS) and TNF/ interferon-gamma (TNF/IFN-γ) stimulated pMBMEC monolayers under physiological flow over 161 timeframes (27 minutes). The $CD8^+$ T cells were slightly different in size and appearance when compared to the $CD4^+$ T cells used for training the segmentation model. To benchmark our established ^{UFM}Track pipeline in this more difficult configuration, the datasets were first manually analyzed by four experimenters: one advanced experimenter with four years of experience (AdEx) and three inexperienced experimenters who received comparable 2-hour introduction and training (Ex1-Ex3). The analyses were performed on the subset of the acquisition, 161 timeframes long starting from timeframe 31.

Manual cell analysis and tracking were performed as described in the “Materials and Methods” section separately for each of the 8 tiles of the tiled acquisition. Next, all crawling $CD8^+$ T cells that did not perform transmigration were manually tracked for the timespan after the flow was increased to the physiological level using the manual tracking in ImageJ.

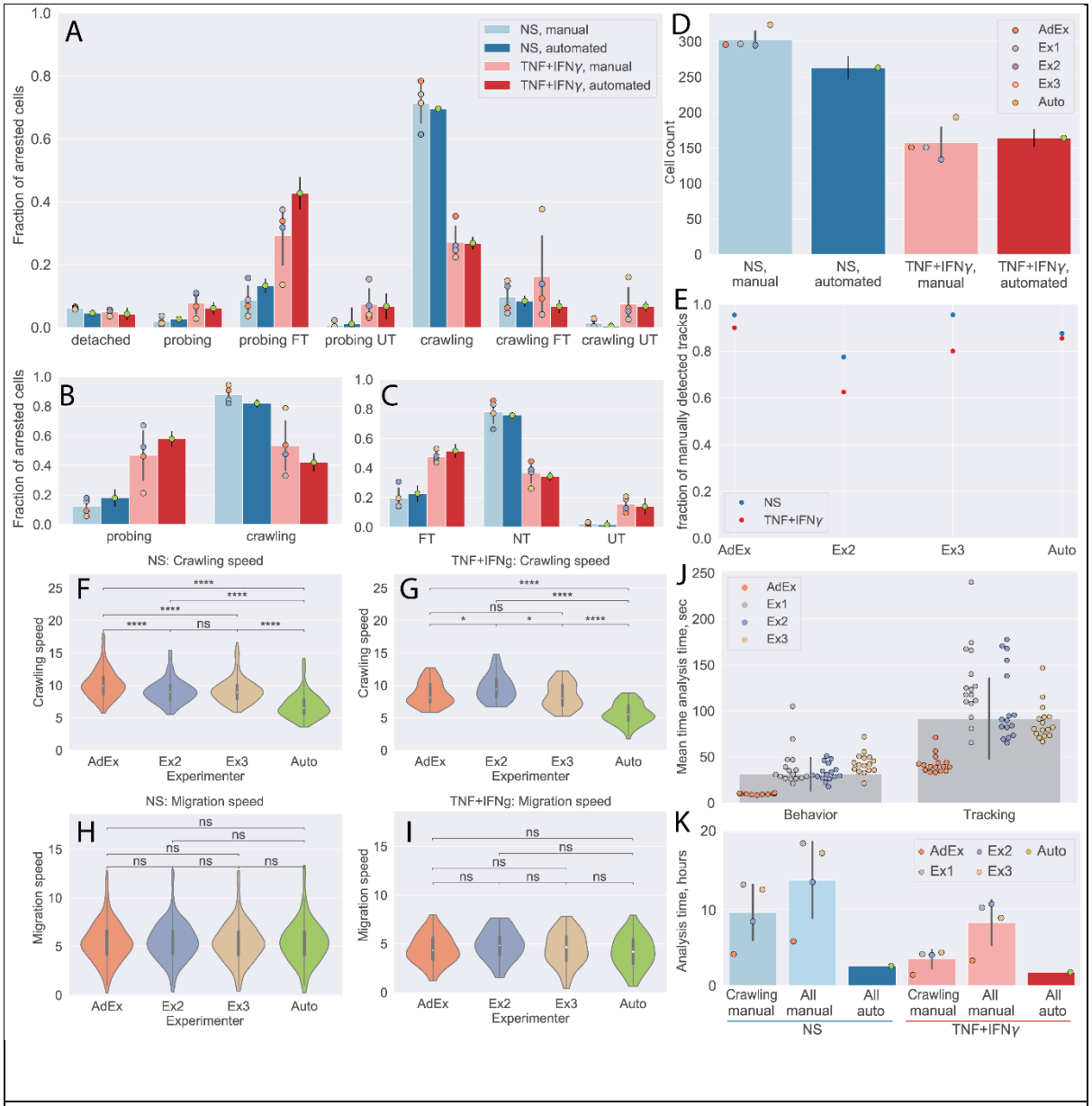

Figure 5. Comparison of automated analysis with ^{UFM}Track and manual analysis of the CD8^{+} T-cell tracks. A-C: CD8^{+} T-cell behavior statistic obtained for non-stimulated (NS) and cytokine-stimulated pMBMECs as obtained manually by four experimenters, as well as automatically with ^{UFM}Track. A. Quantification of CD8^{+} T-cell behavior in the respective categories obtained on non-stimulated and TNF/IFN-γ stimulated pMBMECs is consistent with results obtained by manual frame-by-frame analysis. Cytokine stimulation of pMBMECs increases T-cell probing behavior (B) and T-cell transmigration rate (C). Error bars show the standard deviation of the manual analysis and the statistical error of the mean for automated analysis. Points correspond to individual experimenters.

D. Counts of CD8$^+$ T cells were obtained manually by four experimenters and automatically by ^{UFM}Track. The T-cell detection efficiency is above 90%. Error bars show the standard deviation of the manual analysis and the statistical error of the mean for the automated analysis. Points correspond to individual experimenters. E. Detection efficiency of crawling CD8$^+$ T cell tracks between the manual and automated analysis. F-I. Comparison of CD8$^+$ T-cell crawling speed (path/time) (F, G) and migration speed (displacement/time) (H, I) on non-stimulated (F, H) and cytokine-stimulated (G, I) pMBMECs. The T-cell position assignment error in manual tracking leads to biased crawling speed estimation. J. Comparison of the analysis time (per cell) required for behavior analysis and tracking of CD8$^+$ T cells. K. Total analysis time (per dataset) for behavior analysis and tracking of CD8$^+$ T cells. Comparison is shown for manual analysis with tracking of crawling cells only (Crawling manual), the time estimate for manual analysis with tracking of all cells (All manual), and the in-depth automated analysis of all cell tracks with ^{UFM}Track (All auto).

FT - T cells performed full transmigration; UT – T cells performed uncompleted transmigration; NT - T cells did not perform transmigration.

First, we compared the CD8$^+$ T cell behavior statistics obtained manually and by our automated analysis pipeline (Figure 5A-C). The results obtained by the automated analysis were in full agreement with the manual analysis performed by the experienced experimenter. At the same time, the data highlight the variability of the results from the inexperienced experimenters, confirming the potential for significant experimenter bias.

We also show the detection efficiency of T cells by the ^{UFM}Track. To achieve this goal, we combined the numbers of CD8$^+$ T cells detected in each tile by manual analysis. Due to the overlap between the individual tiles, some CD8$^+$ T cells are seen more than once. To obtain an estimate of the total CD8$^+$ T cell count detected manually, we scaled the number of CD8$^+$ T cells accordingly to the number of detected unique T-cell tracks (see below). By this approach, we found T-cell detection efficiency to be above 90% (Figure 5D). The increased T-cell density can explain lower efficiency in

355 the NS condition. These findings set the appropriate T-cell density for automated analysis of their
356 migration behavior on pMBMEC monolayers to 200-300 cells per FoV of the size of 3.8 mm^2 or 50-80
357 cells/mm^2.

358 Next, we compared the T-cells tracks as obtained manually by three experimenters as well as
359 automatically by our ^{UFM}Track. To this end, we first matched the tracks in adjacent tiles to obtain the
360 tracks on the whole imaging area, avoiding multiple counts of the same track. This was achieved by
361 pattern matching with initial offsets between tiles obtained by an automatic frame alignment
362 procedure performed as part of the automatic analysis. We considered T-cell tracks observed in
363 different tiles to be tracks of the same T cell if $f_{in} > \frac{1}{2} f_{out} - 0.8$, where f_{in} is the fraction of
364 timepoints along a track at which the distance between the T cells was below 17 µm and f_{out} was
365 the fraction of timepoints along a track at which distance between cells was above 25 µm. We used
366 the same approach to match the T-cell tracks obtained by each experimenter and the automated
367 ^{UFM}Track. To compare performance in an objective manner, we excluded manually obtained tracks
368 that lay outside of the fiducial volume of the automated analysis, as well as T cells that were
369 touching another T cell at the end of the acquisition, as those were also excluded from the
370 automated analysis. We then took as 100% the sum of all T-cell tracks detected manually. We
371 evaluated the fraction of all T-cell tracks detected by each experimenter as well as automatically by
372 our ^{UFM}Track.

373 In Figure 5E, we show that our pipeline achieves a comparable T-cell tracking efficiency when
374 compared to the manual analysis. While its performance was not superior to that of the
375 experimenter with four years of expertise in the analysis of the under-flow datasets, it does perform
376 better than less experienced experimenters.

377 We also compared the T-cell motility parameters obtained manually and automatically for the
378 non-stimulated and stimulated pMBMECs (Figure 5F-I). Data obtained for the $CD8^+$ T-cell migration
379 speed on pMBMECs was comparable between all experimenters and the automated analysis. In

380 contrast, results obtained for the T-cell crawling speed were significantly different between the
381 automated approach and manual analysis. Taking a closer look at the T-cell tracks (Supplementary
382 Figure 6), we readily observed that the manual analysis contains significant errors in the assignment
383 of the T-cell position. This leads to a jittery pattern in the T-cell migration tracks and overestimating
384 the T-cell path and, thus, T-cell crawling speed. Employing our novel automated analysis pipeline
385 eliminated this systematic error in the measurements.

386 To finally investigate the potential benefit in the time required for automated versus manual data
387 analysis, we examined the time required for a given experimenter to analyze such datasets manually
388 using the Clockify time tracker (22). In Figure 5J, we show the average time investment needed to
389 perform a complete T-cell behavior analysis and T-cell tracking in each imaging tile, as well as on
390 average. Clearly, the experienced experimenter outperforms the inexperienced experimenters by a
391 factor of 3. On average, a researcher would thus spend 8.1 hours analyzing a dataset with 300 T cells
392 when only the tracks of crawling T cells (50%, i.e., 150 cells) are analyzed. If all T-cell tracks were to
393 be analyzed, this time would further increase to 12.9 hours. Given that on average 10 datasets can
394 be produced per day, manual analysis becomes a bottleneck, leading to delays in exhaustive data
395 analysis and thus ultimately in research progress. The ^{UFM}Track framework reduces analysis time by a
396 factor of 3 when analyzing only crawling cells and 5 if all cell tracks are to be analyzed (Figure 5K).
397 With an average analysis time of 2.3 hours, the 10 experiments carried out in one day can be
398 thoroughly analyzed within one day of machine time. This enables the scalability of flow-based
399 immune cell migration experiments while simultaneously lifting the burden of tedious and time-
400 consuming manual analysis from the researchers.

401

402 V. Applicability of ^{UFM}Track to different models of immune cell - endothelial cell interactions

403 To assess the broader applicability of the ^{UFM}Track framework to different cell types and BBB
404 models employed for the *in vitro* under-flow cell trafficking assays. To this end, we have performed

405 the automated analysis of the multi-step T-cell migration cascade in a set of datasets (one to eight)
406 across different cell types and assays. Specifically, we attempted to verify the feasibility of analysis of
407 datasets where the cells forming the monolayer or the migrating cells have noticeably different
408 appearances, cells from other species are used, specifically human-derived cells, and datasets with a
409 different imaging modality. These include human peripheral blood mononuclear cells (hPBMCs),
410 human T cells, bone marrow-derived macrophages (BMDM) interacting with a monolayer of mouse-
411 and human-derived brain microvascular endothelial cells as well as with immobilized recombinant
412 BBB adhesion molecules (See "Material and Methods" section for details). To assess the
413 performance of the model in each condition, we have performed a visual inspection of the cell
414 masks, transmigration masks, and cell tracks for few datasets in each assay type. We then analyzed
415 cell behavior distribution or motility parameters relevant in each case.

416

417 1. hPBMC on HBMEC monolayer

418 The interaction of hPBMCs with the BBB is altered under different disease conditions. We have
419 therefore analyzed a dataset of human PBMCs on human brain microvascular endothelial cells
420 (HBMEC) to quantify the cell behavior statistic. While the endothelial cells look significantly different
421 than the pMBMECs, the segmentation and transmigration detection quality was sufficient to
422 perform the cell migration analysis. This was also confirmed by the visual inspection of the cell and
423 transmigration masks and cell tracking results (Figure 6 A). We then quantified the PBMC behavior
424 distribution and the crawling and migration speed of the crawling PBMC (Figure 6 B, C).

425 2. BMDM on the pMBMEC monolayer

426 Invasion of macrophages into the CNS contributes to many neurological disorders. Therefore, we
427 have explored if ^{UFM}Track also allows us to analyze the interaction of BMDMs with the BBB under
428 physiological flow in vitro. To this end, we have analyzed two datasets of mouse BMDMs interacting

429 with pMBMEC monolayers (Figure 6 D). Despite the different behavior and appearance of the
430 macrophages as compared to the T cells, the segmentation quality was sufficient to perform the cell
431 tracking and analyze cell motility parameters (Figure 6 E, F), as confirmed by visual inspection of the
432 macrophages masks and cell tracking results (Figure 6 D). Nonetheless, due to the different
433 appearance of the flattening crawling cells and the transmigrated cells, the transmigration detection
434 trained on the mouse T cells does not perform sufficiently well for the robust detection of
435 transmigrating macrophages.

436 3. Human T cells on EECM-BMEC monolayer

437 Next, we analyzed eight datasets of human T cells interacting with the human induced pluripotent
438 stem cell (hiPSC) derived extended endothelial cell culture method brain microvascular endothelial
439 cell (EECM-BMEC)-like cell monolayers (Figure 6 G). EECM-BEMCs establish barrier properties
440 comparable to primary human BMECs and display a mature immune phenotype allowing to perform
441 studies for the first time in a fully autologous manner of immune cell interactions with patient-
442 derived in vitro models of the BBB (23). Despite the cells being of different species, the T cells were
443 successfully segmented, and their transmigration was detected, as confirmed by visual inspection of
444 the T-cell and transmigration masks and cell tracking results (Figure 6 G).

445 We have confirmed the differences in migration statistics (Figure 6 J, K), migration and crawling
446 speed of the crawling T cells (Figure 6 H), as well as the previously reported difference in relative
447 (normalized to track pathlength) displacement (Figure 6 I) of the T cells treated with anti-α4-integrin
448 + anti-β2-integrin blocking antibodies (bab) and control (ctrl) condition (24).

449 4. Human T cells on immobilized recombinant BBB adhesion molecules

450 Finally, we have analyzed datasets acquired in a different imaging modality. Seven datasets of
451 human T cells interacting with immobilized recombinant BBB adhesion molecules, namely ICAM-1,
452 VCAM-1, and their combination (Figure 6 l). In this case, the fluorescently labeled cells were imaged

with epi-fluorescent microscopy. In the absence of a monolayer, transmigration detection is not necessary. Thus we performed cell segmentation directly on the fluorescent signal (See Materials and Methods for details) using the same segmentation strategy as for the T-cell masks. The tracking was then performed the same way as for other experiments. The T cells were successfully segmented and tracked, as confirmed by visual inspection. We compared T cell behavior and motility parameters for three conditions of the recombinant adhesion molecules: ICAM-1, VCAM-1, and ICAM1 + VCAM1 (Figure 6 M, O). Consistent with previous observations (11,24), we observed that in the absence of ICAM-1, T cells were moving in the direction of flow (Figure 6 N).

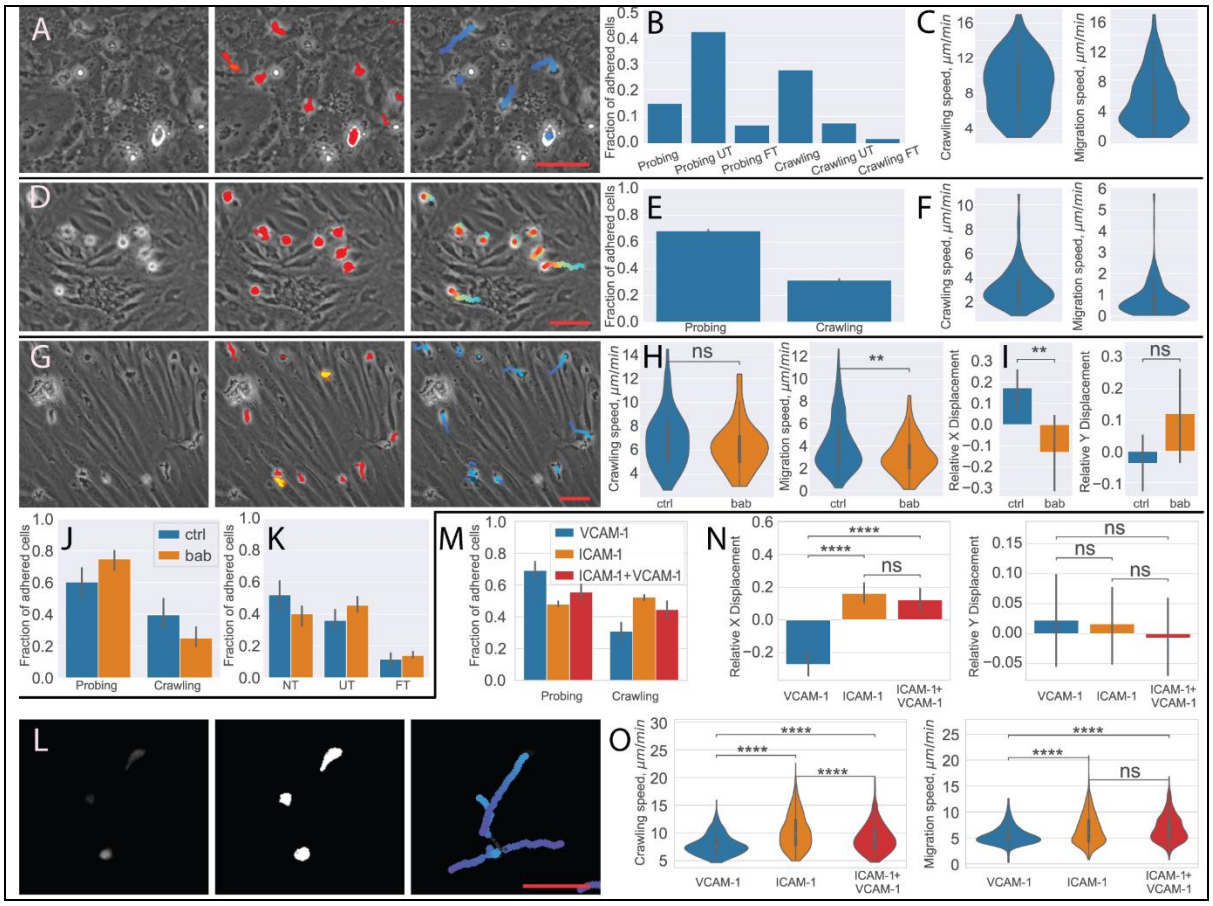

Figure 6. Analysis of different BBB models with ^{UFM}Track. A-C. Human PBMCs interacting with HBMEC. A. Raw image frame, segmentation, and tracking results. B. PBMCs behavior distribution. C. Crawling and migration speed distribution. D-F. BMDM interacting with the pMBMEC monolayer. D. Raw image frame, segmentation, and tracking results. E. BMDM crawling vs probing behavior distribution. F. Crawling and migration speed distribution. G-K. Human T cells interacting with the EECM BMEC monolayer. G. Raw image frame, segmentation, and tracking results. H. Crawling and migration speed distributions for the control condition (ctrl) and with the blocking anti-bodies (bab). I. X and Y relative cell displacement. J. Crawling vs probing behavior comparison. K. Transmigrations behavior comparison. L-O. Human T cells interacting with immobilized recombinant BBB adhesion molecules. L. Raw fluorescent image frame, thresholding-based segmentation, and tracking results. M. Crawling vs probing behavior distribution. N. X and Y relative displacement O. Crawling vs probing speed comparison.

Scale bar 50 µm. Statistical tests are performed with the Mann-Whitney U test.

Discussion

In this study, we have developed the under-flow migration tracker (^{UFM}Track) framework. It consists of independent modules and allows for segmentation, tracking, and motility analysis of T cells, migrating on, across, and below the monolayer of primary mouse brain microvascular endothelial cells under physiological flow in vitro. The developed method relies exclusively on phase-contrast imaging data. Therefore, it does not require establishing fluorescent labels of the migrating immune cell population to be studied, avoids potential photo-toxicity to be considered for fluorescent imaging modalities (25–27), and is thus the preferred choice for analyzing the trafficking of sensitive cell types. T-cell segmentation and prediction of the transmigrated T-cell areas are performed using a custom 2D+T U-Net-like convolutional neural network. It enables reliable segmentation of T cells both above and below the pMBMEC monolayer. The existing particle and cell

474 tracking toolkits consider migration of one cell type and thus are not suitable for the detection of
475 distinct migration regimes and cell interactions (28–31). Furthermore, to our knowledge, none of the
476 existing algorithms consider migration under the flow causing rapid cell displacement. The tracking
477 of T-cell interactions with the pMBMECs during all migration regimes under physiological flow
478 required designing a new tracking algorithm considering rapid T-cell appearance, disappearance, and
479 displacement in the field of view caused by the flow. We have also developed approaches that
480 resolve track intersections, i.e., identifying track segments corresponding to the same T cell before
481 and after under-segmented track regions, which are inevitable during T-cell migration. By
482 establishing the detection of T-cell crawling, probing, transmigration, and accelerated movement
483 combined with reliable T-cell tracking, we have enabled the in-depth analysis of distinct migration
484 regimes on a cell-by-cell basis. By reducing the dataset analysis time by a factor of 5, ^{UFM}Track allows
485 for performing a thorough analysis of 10 experiments that a researcher can carry out in one day
486 within one day of machine-time. We have demonstrated that the automated analysis performs on
487 par with manual analysis while improving accuracy and eliminating experimenter bias, and enables
488 scalability of flow-based immune cell migration experiments by reducing the analysis cost and lifting
489 the burden of time-consuming manual analysis.

490 In this work, we have demonstrated the applicability of the developed framework to the analysis
491 of the multi-step extravasation of $CD4^+$ and $CD8^+$ T cells across non-stimulated or cytokine-
492 stimulated pMBMEC monolayers under physiological flow. We have also demonstrated that the
493 developed framework allows for automated analysis of T-cell behavior statistics and motility
494 parameters of distinct T-cell migration regimes. Results of the automated analysis of $CD4^+$ T-cell
495 behavioral statistics performed with ^{UFM}Track are in agreement with previous studies using manual
496 data analysis (13). The automated analysis of datasets of $CD8^+$ T-cell migration has shown
497 comparable performance with manual analysis performed by one experimenter with four years of
498 analysis experience and three less-experienced experimenters. At the same time, the variance of the
499 results obtained manually showed significant experimenter bias that the automated analysis

500 eliminated. Additionally, the automated analysis allowed for in-depth analysis of all T-cell migration
501 categories and precise evaluation of T-cell motility parameters, which was not achieved by manual T-
502 cell tracking, even by the most experienced user.

503 We have further demonstrated the applicability of the UFMTrack framework to the analysis of
504 different cell types (BMDM, PBMC), species (human-derived T cells, HBMEC, and EECM BMEC) as
505 well as tracking and analysis of cell migration imaged using the fluorescent imaging modality. In all
506 cases, the cells could be successfully segmented and tracked, and the cell migration analysis was
507 performed on a cell-by-cell basis. In the case of the BMDMs, which have significantly different
508 appearances during transmigration from the T cells, reliable transmigration detection was not
509 obtained, yet the motility parameter evaluation was successful. For all the other analyzed cell types,
510 the cell segmentation and transmigration detection model trained on the annotated $CD4^+$ T cells also
511 produced transmigration maps of sufficient quality for reliable transmigration detection.

512 Quantifying the fraction of transmigrated T cells is crucial for studying the molecular mechanisms
513 governing the infiltration of autoaggressive T cells across the BBB into the CNS parenchyma and the
514 immune surveillance. The role of specific endothelial or T-cell adhesion molecules in influencing the
515 dynamic interactions of T cells with pMBMECs can, e.g., be probed by quantifying the ratio of T-cell
516 crawling behavior to T-cell probing. With the analysis procedure established in the UFMTrack
517 framework, the number of times a T cell interrupts its crawling regime by switching to short probing
518 behavior on the endothelium can be evaluated, thus providing information on the distribution of
519 “hot spots” on the endothelium. Additionally, experiment scalability and the analysis on a cell-by-cell
520 basis enable the search for distinct populations of T-cells, e.g., according to the distribution of
521 probing to crawling behavioral ratios. The strength of T-cell adhesion to the endothelium can be
522 probed with the developed framework using the measure of T-cell detachment rate and the
523 distribution of the previously overlooked T-cell accelerated movement occurrences and accelerated
524 movement speed. Finally, the possibility of quantifying the motility parameters of the transmigrated

525 T cells enables future studies involving multilayer in vitro BBB models that include the vascular
526 basement membrane in addition to mural cells such as pericytes and astrocytes mimicking the entire
527 neurovascular unit.

528 While in this work we have focused primarily on the analysis of mouse T cells interacting with
529 pMBMEC under flow or other immune cells interacting with the endothelial monolayer, the methods
530 we present establish a foundation for a broad range of studies involving in vitro under-flow studies
531 of immune cell trafficking. The tracking algorithm and motility analysis developed in the ^{UFM}Track
532 framework are also directly applicable to the analysis of immune cell interactions with recombinant
533 BBB adhesion molecules under flow. In this case, either phase-contrast or epi-fluorescent imaging
534 can be employed when studying fluorescently labeled immune cells, as demonstrated. The T-cell
535 segmentation based on deep neural networks can be applied to studies of the trafficking of other
536 immune cell subsets on and across the pMBMEC monolayer. We demonstrated the successful
537 application of the ^{UFM}Track to cells with significantly different appearances, such as the HBMEC
538 cellular monolayers. The application to immune cell trafficking across other endothelial monolayers,
539 including those from different species or vascular beds as well as lymphatic endothelial cells where
540 the cell appearance is drastically different from the ones demonstrated here, is possible but requires
541 fine-tuning of the trained segmentation model. While training the models presented here required a
542 large dataset of annotated T-cell masks, and transmigration masks, this can be largely avoided for
543 future development. Future models can be developed more efficiently by leveraging our existing
544 annotated dataset of T-cell migration on the pMBMECs while employing transfer learning
545 approaches in a multitask framework with weak supervision and fluorescent labels as auxiliary
546 learning targets to adapt the model for the segmentation of cells with different appearances. This
547 can be further improved by adopting self-supervised contrastive learning methods, which have
548 demonstrated significant advancements in model pretraining in recent years. This is the subject of
549 our future studies. By sharing the data and open-source code of the ^{UFM}Track framework, i.e., the
550 training data used for the segmentation model training, trained models, as well as the model

551 architecture, and full under-flow T-cell tracking and migration analysis pipeline, we hope to
552 encourage the community to pursue these developments to advance the field.

553 One current limitation of the method is the performance reduction of the T-cell tracking when
554 the density of migrating T cells significantly increases (>250 cells/dataset). Thus, the recommended T
555 cell concentration is about 100-150k/ml. However, to avoid non-physiological interactions between
556 migrating T cells and T cell clumping, the T-cell density should be kept at moderate levels anyway.
557 Additionally, analyzing data from 8 stitched FoVs allows for obtaining comparable statistics. The
558 current analysis of the behavioral statistics quantifies the fraction of different T-cell migration
559 regimes with respect to the number of adhered cells instead of the total T-cell count passing through
560 the microfluidic device. While the number of fast-moving T cells during the accumulation phase
561 cannot be directly counted using the imaging modality employed here, it can be estimated indirectly
562 from the imaging data with additional calibration experiments and a dedicated machine learning
563 model. Another limitation is that currently, we do not consider dividing immune cells. While cell
564 division events happen rarely (<1% of T cells) and are not primary events for the study of immune
565 cell interaction with the BBB model, the modular architecture of our framework will facilitate future
566 extension to detect cell division.

567 By enabling experiment scalability, unbiased analysis with advanced accuracy, and an in-depth
568 analysis of large datasets of T-cell dynamics under flow, the computational and analytical framework
569 presented here contributes to the 3R principle when studying the interaction of cells derived from
570 animal models by reducing the number of animals to be sacrificed. ^{UFM}Track can be employed for
571 fundamental research of the molecular mechanisms governing immune cell trafficking across a range
572 of vascular beds, screening of pharmaceutical treatments, as well as for personalized medicine
573 based on the evaluation of treatment efficacy on patient-derived T-cell migration behavior on
574 patient-derived endothelial monolayers. Eventually, the developed framework can be extended to
575 real-time operation during image acquisition. Combined with transgenic photo-convertible immune

576 cells allowing for the photoconversion of immune cells according to their behavior will allow for
577 subsequent fluorescent cell sorting and scRNA-Seq analysis. Such advanced studies are needed to
578 reveal the role of genetic differences governing T-cell migration regimes.
579
580

581 Materials and Methods

582 1. pMBMEC cell culture

583 Primary mouse brain microvascular endothelial cells (pMBMECs) were isolated from 8-12 weeks
584 old C57BL/6J WT mice and cultured exactly as described before (11,32). Intact monolayers were
585 stimulated or not with 10 ng/mL of recombinant mouse TNF, 20 ng/mL of recombinant mouse IL1-β
586 for, or 5ng/mL recombinant mouse TNF + 100 U/mL recombinant mouse IFN-γ 16-24 hours prior to
587 the assays as previously described (20).

588

589 2. Human brain microvascular endothelial cells

590 Human brain microvascular endothelial cells (HBMEC) were kindly provided by Prof. Nicholas
591 Schwab (University of Münster, Germany). They were cultured to confluency on speed coating
592 solution coated µ-Dishes (35 mm, low, iBidi) for 2 days as previously described (20).

593

594 3. Extended endothelial culture method—brain microvascular endothelial cell-like cells

595 The Extended Endothelial Cell Culture Method (EECM) was used to differentiate human induced
596 pluripotent stem cells (hiPSCs) to brain microvascular endothelial cell (BMEC)-like cells were
597 employed as a human in vitro model of the BBB. In brief, hiPSCs from one healthy control (HC) (cell
598 line ID: LNISi002-B) were established from erythroblasts in the laboratory of Renaud DuPasquier
599 (University of Lausanne, Switzerland). EECM-BMEC-like cells were cultured to confluency on collagen
600 IV and fibronectin-coated µ-Dishes (35 mm, low, iBidi) for 2 days (24).

601

602 4. T cell and hPBMC preparation

603 Naïve $CD4^+$ and $CD8^+$ T-cell isolation: Peripheral lymph nodes and spleens from 2D2 and OT-I
604 C57BL/6J mice were harvested, and single-cell suspensions were obtained by homogenization and
605 filtration through a sterile 100 μm nylon mesh. A second filtration was applied after erythrocyte lysis
606 (0.83% NH4Cl, Tris-HCl). 2D2 and OT-I cells were isolated respectively with magnetic $CD4^+$ and $CD8^+$ T
607 cell selection beads (EasySep, STEMCELL Technologies).

608 In vitro activation of naïve $CD8^+$ T cells: OT-I $CD8^+$ T cells were activated as described before
609 (33,34). Activated $CD8^+$ T cells were cultured in IL-2-containing media for 3 days post-activation.

610 In vitro activation of naïve $CD4^+$ T cells: 2D2 $CD4^+$ T cells were activated as described before (20).
611 Activated $CD4^+$ T cells were cultured in IL-2-containing media for 24 additional hours.

612 hPBMC were isolated from buffy coats of healthy donors by Ficoll-Paque™ Plus (Cytiva) density
613 gradient and were frozen and stored in a liquid nitrogen tank until use as previously described in
614 (24).

615 Human $CD4^+$ T cells were isolated by employing a $CD4^+$ T cells isolation kit (Miltenyi Biotec kit)
616 following the provider's instructions. Subsequently, effector/memory $CD4^+$ T cells were sorted by
617 Fluorescence-Activated Cell Sorting (FACS) into different Th subsets according to their specific
618 surface expression of chemokine receptors ($CCR6^-CXCR3^+CCR4^-$ for Th1; $CCR6^+CXCR3^+CCR4^-$ for
619 Th1*; $CCR6^-CXCR3^-CCR4^+$ for Th2; $CCR6^+CXCR3^-CCR4^+$ for Th17) and expanded as previously
620 described (2,21,35–38).

621

622 5. BMDM preparation

623 BMDMs were prepared as described in (Berve et al., manuscript in preparation). In brief, the
624 mouse bone marrow was harvested and washed through a 100 µm nylon mesh. After 7 days of cell
625 culture were plated in a density of 17-20 × 10^6 cells/mL in BMDM medium supplemented with
626 5ng/mL of recombinant mouse macrophage colony stimulating factor (mCSF, R&D Biosystems,

627 Minneapolis, USA, 416-ML-500) onto non-treated 100mm tissue culture Petri dishes (Greiner Bio-
628 One, St. Gallen, Switzerland) for 7 days at 37°C and 5% CO_2 the cells were harvested by incubation
629 with 0.05% Trypsin.

630

631 6. T cell binding assays under physiological flow conditions

632 For live-cell imaging of T-cell interaction with recombinant BBB cell adhesion molecules under the
633 physiological flow condition, µ-Dishes (35 mm, low, iBidi) were coated with 1.54 µg/mL human
634 recombinant VCAM-1 (Biolegend) and/or 1.14 µg/mL human recombinant ICAM-1 (R&D system) in
635 DPBS for 1 h at 37°C and blocked with 1.5% (v/v) bovine serum albumin (Sigma-Aldrich) in DPBS
636 overnight at 4°C.

637 CMFDA prelabelled Th cells were incubated with the isotype control antibody (30 µg/mL) for 30
638 minutes at 37°C (8% CO_2) prior to imaging (exact antibody concentrations are illustrated in the figure
639 legend). The cells were subsequently perfused on top of the pre-coated dishes at a concentration of
640 10^6/mL in MAM as previously described (11,24).

641

642 7. In vitro under-flow T-cell migration assay

643 We studied the multi-step T-cell migration across monolayers of primary mouse brain
644 microvascular endothelial cells (pMBMECs) in a microfluidic device under physiological flow by in
645 vitro live-cell imaging according to the previously established procedure (13,20). A custom-made
646 flow chamber was placed on top of the pMBMECs, previously cultured in Ibidi µ-Dish to confluency,
647 and connected to the flow system filled with migration assay medium (MAM) (11). During the
648 accumulation phase, T cells at a concentration between 55k/mL and 166k/mL were perfused on top
649 for 5 minutes under low shear stress of 0.1 dynes/cm^2 allowing them to settle on top of the
650 pMBMEC monolayer. We used lower T-cell concentration compared to previous studies to enable

651 automated T-cell interaction analysis. Afterward, the flow was increased to physiological levels with
652 a flow shear stress of 1.5 dynes/cm^2 to study post-arrest T-cell behavior on pMBMECs for 27 minutes
653 (Figure 1A, B).

654

655 8. Data acquisition

656 The timelapse imaging was performed during both accumulation and physiological flow phases
657 using phase-contrast imaging at a framerate of 6 frames/minute or 12 frames/minute, subsampled
658 to 6 frames/minute and resolution of 0.629 µm/pixel with a 10x objective. In this modality the
659 acquired images are gray scale, and the T cells, especially after the migration across the pMBMEC
660 monolayer, have a similar appearance to the pMBMECs, making the T-cell segmentation task very
661 challenging (Figure 1C). The data was acquired in tiles of 870 × 650 µm^2 (1389 × 1041 pixels) with an
662 overlap of 100 µm, leading to a total acquired image area of 3170 × 1220 µm^2. For each experiment,
663 the dataset consists of 30 timeframes of T-cell accumulation and 162 timeframes of dynamic T-cell
664 interactions with the pMBMEC monolayer under physiological flow. The timestep between
665 sequential timeframes for each tile is 10 s. The total acquired area is thus limited by the acquisition
666 speed or by the flow chamber size.

667 The HBMEC dataset was acquired as previously described (24). In brief, 2 tiles were acquired of
668 total size 3891 × 1504 pixels with pixel size 0.69 µm and framerate 6 frames/minute. The
669 accumulation phase was 4 minutes, and the physiological flow phase was 5 minutes.

670 The BMDM dataset was acquired similarly to the T cell interacting with the pMBMEC datasets. In
671 brief, one tile was acquired of size of 2048 × 1504 or 1388 × 1040 pixels with pixel size 0.69 or
672 0.629 µm and framerate 6 frames/minute. The accumulation phase lasted 6 minutes, and the
673 physiological flow phase was 25 minutes.

674 The EECM-BMEC dataset was acquired as previously described (24). In brief, 2 tiles were acquired
675 of total size 3892 × 1504 or 2638 × 1048 pixels with pixel size 0.69 or 0.629 µm and framerate
676 6 frames/minute.

677 The dataset of human T cells on immobilized recombinant BBB adhesion molecules was acquired
678 as previously described (24). In brief, 2 tiles were acquired of total size 3891 × 1504 pixels with pixel
679 size 0.69 µm and framerate 6 frames/minute. The accumulation phase was 4 minutes, and the
680 physiological flow phase was 5 minutes. In this dataset, there is only one compartment, thus
681 excluding any transmigration of the T cells. We, therefore, have employed the preprocessed
682 fluorescent images instead of the cell probability map and transmigration map produced by the
683 segmentation neural network. In this case, the centroids are defined as local maxima localized on
684 the preprocessed fluorescent images. The fluorescent images were preprocessed first by performing
685 Gaussian blur filtering in 2D with a standard deviation of 0.75. Next, thresholding was applied to
686 eliminate the background noise, clipping high brightness values (color values with abundance <0.3%
687 of threshold abundance), scaling to 0-255 8 bit, and saving in a lossless format. Finally, the 2 tiles
688 were stitched together by matching the integrated color distribution in the X direction in the
689 overlapping area.

690

691 9. Manual analysis of T-cell migration

692 Manual cell analysis and tracking were performed according to the previously established
693 procedure using ImageJ software (ImageJ software, National Institute of Health, Bethesda, MD, USA)
694 (12). The number of arrested T cells was thus counted at timeframe 33 of the subset. The behavior
695 of arrested T cells was defined and expressed as fractions of arrested T cells set to 100% as follows:

696 - T cells that detached during the observation time ("detached")
697 - T cells that migrated out of the FoV detached during the observation time ("out of FoV")
698 - T cells that continuously crawled on the pMBMEC monolayer ("crawling")

699 • T cells that remained in the same location (displacement less than twice the cell size) while
700 actively interacting with the pMBMEC monolayer ("probing")
701 • T cells that crossed the pMBMEC monolayer with or without prior crawling ("crawling full
702 transmigration" and "probing full transmigration"). The event of T-cell transmigration across the
703 pMBMECs monolayer became obvious due to the change of appearance of the transmigrated part of
704 the T cells from phase bright (on top of the pMBMECs monolayer) to phase dark.
705 • T cells that partially crossed the pMBMEC monolayer, then retracted the protrusions and
706 continued to migrate above the monolayer ("crawling uncompleted transmigration" and "probing
707 uncompleted transmigration").
708
709 10. ^{UFM}Track performance evaluation

710 The inference of T cell masks and transmigration masks was performed on a dual-CPU Intel(R)
711 Xeon(R) CPU E5-2670 v3 @ 2.30GHz, 256GB RAM node equipped with 8 Graphical Processing Units
712 (GPU) NVIDIA GeForce GTX TITAN X / GeForce GTX 1080. Frame alignment and segmentation were
713 performed on an Intel(R) Core(TM) CPU i7-4771 @ 3.50GHz, 32GB RAM workstation with NVIDIA
714 GeForce GTX TITAN GPU. Cell tracking was performed on a dual-CPU Intel(R) Xeon(R) CPU E5-2643
715 v2 @ 3.50GHz, 256GB RAM workstation.

716

717 Acknowledgments

718 We thank Kristina Berve for providing BMDM datasets for analysis with the ^{UFM}Track. We owe
719 sincere thanks to Dr. James McGrath and Danial Ahmad (Rochester University, NY, USA) for their
720 detailed and insightful feedback on our manuscript. This work was supported by an UniBe ID Grant
721 to MV, BE, and AA and the Microscopy Imaging Center (MIC) of the University of Bern.

722

Data Availability

The source code for the T-cell segmentation models, data preprocessing, training, performance evaluation, and inference scripts are available on GitHub at https://github.com/neworldemancer/UFMSegm. This repository also contains win64 binaries used for the watershed-based segmentation of the predicted T cell probability maps and transmigration probability maps.

The source code for the under-flow T-cell tracking and migration analysis, along with the scripts used for performance evaluation of the framework, is available on GitHub at https://github.com/neworldemancer/UFMTrack.

The training phase-contrast data with manual annotations, the reference datasets for histogram normalization, and trained models are available on Zenodo: [http://doi.org/10.5281/zenodo.7489557].

The datasets used for evaluation of our framework are available on Zenodo: [http://doi.org/10.5281/zenodo.7489972, http://doi.org/10.5281/zenodo.7489984, http://doi.org/10.5281/zenodo.7489996, http://doi.org/10.5281/zenodo.7490012, http://doi.org/10.5281/zenodo.7490020, http://doi.org/10.5281/zenodo.7490029].

References

1. Marchetti L, Engelhardt B. Immune cell trafficking across the blood-brain barrier in the absence and presence of neuroinflammation. Vasc Biol [Internet]. 2020 Apr 10 [cited 2022 Oct 28];2(1):H1–18. Available from: https://vb.bioscientifica.com/view/journals/vb/2/1/VB-19-0033.xml

2. Nishihara H, Soldati S, Mossu A, Rosito M, Rudolph H, Muller WA, et al. Human CD4+ T cell subsets differ in their abilities to cross endothelial and epithelial brain barriers in vitro. Fluids

747 Barriers CNS [Internet]. 2020 Feb 3 [cited 2022 Apr 14];17(1):1–18. Available from:
748 https://fluidsbarrierscns.biomedcentral.com/articles/10.1186/s12987-019-0165-2

749 3. Nourshargh S, Alon R. Leukocyte Migration into Inflamed Tissues. Immunity. 2014 Nov
750 20;41(5):694–707.

751 4. Nourshargh S, Hordijk PL, Sixt M. Breaching multiple barriers: leukocyte motility through
752 venular walls and the interstitium. Nat Rev Mol Cell Biol 2010 115 [Internet]. 2010 May [cited
753 2022 Dec 23];11(5):366–78. Available from: https://www.nature.com/articles/nrm2889

754 5. Bartholomäus I, Kawakami N, Odoardi F, Schläger C, Miljkovic D, Ellwart JW, et al. Effector T
755 cell interactions with meningeal vascular structures in nascent autoimmune CNS lesions. Nat
756 2009 4627269 [Internet]. 2009 Oct 14 [cited 2022 Oct 28];462(7269):94–8. Available from:
757 https://www.nature.com/articles/nature08478

758 6. Lyck R, Engelhardt B. Going Against the Tide – How Encephalitogenic T Cells Breach the
759 Blood-Brain Barrier. J Vasc Res [Internet]. 2012 Oct [cited 2020 Mar 10];49(6):497–509.
760 Available from: https://www.karger.com/Article/FullText/341232

761 7. Dias MC, Quesada AO, Soldati S, Bösch F, Gruber I, Hildbrand T, et al. Brain endothelial
762 tricellular junctions as novel sites for T cell diapedesis across the blood-brain barrier. J Cell Sci
763 [Internet]. 2021 Apr 1 [cited 2022 Oct 28];134(8). Available from:
764 https://pubmed.ncbi.nlm.nih.gov/33912914/

765 8. Steinman L, Zamvil SS. Virtues and pitfalls of EAE for the development of therapies for
766 multiple sclerosis. Trends Immunol [Internet]. 2005 [cited 2022 Dec 23];26(11):565–71.
767 Available from: https://pubmed.ncbi.nlm.nih.gov/16153891/

768 9. Singer BA. The role of natalizumab in the treatment of multiple sclerosis: benefits and risks.
769 Ther Adv Neurol Disord [Internet]. 2017 Sep 1 [cited 2022 Dec 23];10(9):327–36. Available
770 from: https://pubmed.ncbi.nlm.nih.gov/28861122/

771 10. Lyck R, Nishihara H, Aydin S, Soldati S, Engelhardt B. Modeling Brain Vasculature Immune
772 Interactions In Vitro. Cold Spring Harb Perspect Med [Internet]. 2022 Dec 12 [cited 2023 Jul
773 19];a041185. Available from:
774 http://perspectivesinmedicine.cshlp.org/content/early/2022/12/12/cshperspect.a041185

775 11. Steiner O, Coisne C, Cecchelli R, Boscacci R, Deutsch U, Engelhardt B, et al. Differential Roles
776 for Endothelial ICAM-1, ICAM-2, and VCAM-1 in Shear-Resistant T Cell Arrest, Polarization,
777 and Directed Crawling on Blood–Brain Barrier Endothelium. J Immunol [Internet]. 2010 Oct
778 15 [cited 2022 Oct 23];185(8):4846–55. Available from:
779 https://www.jimmunol.org/content/185/8/4846

780 12. Rudolph H, Klopstein A, Gruber I, Blatti C, Lyck R, Engelhardt B. Postarrest stalling rather than
781 crawling favors CD8 $^{+}$ over CD4 $^{+}$ T-cell migration across the blood-brain barrier under flow in
782 vitro. Eur J Immunol [Internet]. 2016 Sep 1 [cited 2019 Apr 19];46(9):2187–203. Available
783 from: http://doi.wiley.com/10.1002/eji.201546251

784 13. Abadier M, Jahromi NH, Alves LC, Boscacci R, Vestweber D, Barnum S, et al. Cell surface levels
785 of endothelial ICAM-1 influence the transcellular or paracellular T-cell diapedesis across the
786 blood–brain barrier. 2015 Apr 1 [cited 2019 Apr 19];45(4):1043–58. Available from:
787 http://doi.wiley.com/10.1002/eji.201445125

788 14. Shulman Z, Shinder V, Klein E, Grabovsky V, Yeger O, Geron E, et al. Lymphocyte Crawling and
789 Transendothelial Migration Require Chemokine Triggering of High-Affinity LFA-1 Integrin.
790 Immunity. 2009 Mar 20;30(3):384–96.

791 15. Arts JJG, Mahlandt EK, Grönloh MLB, Schimmel L, Noordstra I, Gordon E, et al. Endothelial
792 junctional membrane protrusions serve as hotspots for neutrophil transmigration. Elife. 2021
793 Aug 1;10.

794 16. Ronneberger O, Fischer P, Brox T. U-Net: Convolutional Networks for Biomedical Image

795 Segmentation. 2015 May 18 [cited 2017 Oct 25]; Available from:
796 http://arxiv.org/abs/1505.04597

797 17. Abadi M, Barham P, Chen J, Chen Z, Davis A, Dean J, et al. TensorFlow: A system for large-
798 scale machine learning. [cited 2022 Oct 23]; Available from: https://tensorflow.org.

799 18. Schiegg M, Hanslovsky P, Kausler BX, Hufnagel L, Hamprecht FA. Conservation Tracking. 2013;

800 19. Perron L, Furnon V. OR-Tools [Internet]. Available from:
801 https://developers.google.com/optimization/

802 20. Haghayegh Jahromi N, Marchetti L, Moalli F, Duc D, Basso C, Tardent H, et al. Intercellular
803 Adhesion Molecule-1 (ICAM-1) and ICAM-2 Differentially Contribute to Peripheral Activation
804 and CNS Entry of Autoaggressive Th1 and Th17 Cells in Experimental Autoimmune
805 Encephalomyelitis. Front Immunol. 2020 Jan 14;10:3056.

806 21. Mossu A, Rosito M, Khire T, Li Chung H, Nishihara H, Gruber I, et al. A silicon nanomembrane
807 platform for the visualization of immune cell trafficking across the human blood–brain barrier
808 under flow. J Cereb Blood Flow Metab [Internet]. 2019 Mar 1 [cited 2022 Dec 21];39(3):395–
809 410. Available from: https://journals.sagepub.com/doi/10.1177/0271678X18820584

810 22. Clockify. Clockify™ - 100% FREE Time Tracking Software [Internet]. 2022 [cited 2022 Oct 23].
811 Available from: https://clockify.me/

812 23. Nishihara H, Gastfriend BD, Kasap P, Palecek SP, Shusta E V., Engelhardt B. Differentiation of
813 human pluripotent stem cells to brain microvascular endothelial cell-like cells suitable to
814 study immune cell interactions. STAR Protoc [Internet]. 2021 Jun 18 [cited 2023 Jun 14];2(2).
815 Available from: https://pubmed.ncbi.nlm.nih.gov/34151293/

816 24. Soldati S, Bär A, Vladymyrov M, Glavin D, McGrath JL, Gosselet F, et al. High levels of
817 endothelial ICAM-1 prohibit natalizumab mediated abrogation of CD4+ T cell arrest on the
818 inflamed BBB under flow in vitro. J Neuroinflammation [Internet]. 2023 May 23 [cited 2023

819 Jun 14];20(1):123. Available from: https://pubmed.ncbi.nlm.nih.gov/37221552/

820 25. Jae Oh D, Min Lee G, Francis K, Palsson BO. Phototoxicity of the Fluorescent Membrane Dyes
821 PKH2 and PKH26 on the Human Hematopoietic KG1a Progenitor Cell Line. [cited 2022 Dec
822 23]; Available from: https://onlinelibrary.wiley.com/terms-and-conditions

823 26. Saetzler RK, Jallo J, Lehr HA, Philips CM, Vasthare U, Arfors KE, et al. Intravital Fluorescence
824 Microscopy: Impact of Light-induced Phototoxicity on Adhesion of Fluorescently Labeled
825 Leukocytes. J Histochem Cytochem. 1997;45(4):505–13.

826 27. Purschke M, Rubio N, Held KD, Redmond RW. Phototoxicity of Hoechst 33342 in time-lapse
827 fluorescence microscopy. Photochem Photobiol Sci [Internet]. 2010 [cited 2022 Dec
828 23];9(12):1634–9. Available from: https://pubmed.ncbi.nlm.nih.gov/20931137/

829 28. Allan DB, Caswell T, Keim NC, van der Wel CM, Verweij RW. Trackpy. 2021 Apr 13 [cited 2022
830 Oct 29]; Available from: https://zenodo.org/record/4682814

831 29. Tsai HF, Gajda J, Sloan TFW, Rares A, Shen AQ. Usiigaci: Instance-aware cell tracking in stain-
832 free phase contrast microscopy enabled by machine learning. SoftwareX. 2019 Jan 1;9:230–7.

833 30. Ershov D, Phan MS, Pylvänäinen JW, Rigaud SU, Le Blanc L, Charles-Orszag A, et al. TrackMate
834 7: integrating state-of-the-art segmentation algorithms into tracking pipelines. Nat Methods
835 2022 197 [Internet]. 2022 Jun 2 [cited 2022 Oct 29];19(7):829–32. Available from:
836 https://www.nature.com/articles/s41592-022-01507-1

837 31. Ulicna K, Vallardi G, Charras G, Lowe AR. Automated Deep Lineage Tree Analysis Using a
838 Bayesian Single Cell Tracking Approach. Front Comput Sci. 2021 Oct 20;3:92.

839 32. Coisne C, Lyck R, Engelhardt B. Live cell imaging techniques to study T cell trafficking across
840 the blood-brain barrier in vitro and in vivo. Fluids Barriers CNS [Internet]. 2013 Jan 21 [cited
841 2020 Mar 9];10(1):7. Available from: http://www.ncbi.nlm.nih.gov/pubmed/23336847

842 33. Rudolph H, Klopstein A, Gruber I, Blatti C, Lyck R, Engelhardt B. Postarrest stalling rather than
843 crawling favors CD8+ over CD4+ T-cell migration across the blood–brain barrier under flow in
844 vitro. Eur J Immunol [Internet]. 2016 Sep 1 [cited 2020 Mar 9];46(9):2187–203. Available
845 from: https://onlinelibrary.wiley.com/doi/full/10.1002/eji.201546251

846 34. Aydin S, Pareja J, Schallenberg VM, Klopstein A, Gruber T, Page N, et al. Antigen recognition
847 detains CD8+ T cells at the blood-brain barrier and contributes to its breakdown. Nat
848 Commun 2023 141 [Internet]. 2023 May 30 [cited 2023 Jul 31];14(1):1–20. Available from:
849 https://www.nature.com/articles/s41467-023-38703-2

850 35. Engen SA, Rukke HV, Becattini S, Jarrossay D, Blix IJ, Petersen FC, et al. The Oral Commensal
851 Streptococcus mitis Shows a Mixed Memory Th Cell Signature That Is Similar to and Cross-
852 Reactive with Streptococcus pneumoniae. PLoS One [Internet]. 2014 Aug 13 [cited 2023 Jun
853 27];9(8):e104306. Available from:
854 https://journals.plos.org/plosone/article?id=10.1371/journal.pone.0104306

855 36. Sallusto F, Lenig D, Mackay CR, Lanzavecchia A. Flexible Programs of Chemokine Receptor
856 Expression on Human Polarized T Helper 1 and 2 Lymphocytes. J Exp Med [Internet]. 1998
857 Mar 16 [cited 2023 Jun 27];187(6):875–83. Available from: http://www.jem.org

858 37. Zielinski CE, Mele F, Aschenbrenner D, Jarrossay D, Ronchi F, Gattorno M, et al. Pathogen-
859 induced human TH17 cells produce IFN-γ or IL-10 and are regulated by IL-1β. Nat 2012
860 4847395 [Internet]. 2012 Apr 1 [cited 2023 Jun 27];484(7395):514–8. Available from:
861 https://www.nature.com/articles/nature10957

862 38. Wimmer I, Tietz S, Nishihara H, Deutsch U, Sallusto F, Gosselet F, et al. PECAM-1 stabilizes
863 blood-brain barrier integrity and favors paracellular T-cell diapedesis across the blood-brain
864 barrier during neuroinflammation. Front Immunol. 2019 Apr 5;10(APR):447986.

865

866

867